

Single-crystal X-ray diffraction and resonant X-ray magnetic scattering at helium-3 temperatures in high magnetic fields at beamline P09 at PETRA III

S. Francoual,^{a*} J. Stempfer,^a J. Warren,^b Y. Liu,^c A. Skaugen,^a S. Poli,^b J. Blume,^a F. Wolff-Fabris,^d P. C. Canfield^{e,f} and T. Lograsso^{c,e}

Received 30 January 2015

Accepted 27 July 2015

Keywords: X-ray diffraction; resonant X-ray magnetic scattering; helium-3 insert cryostat; sub-Kelvin temperatures; X-ray beam heating; single-crystal.

^aDeutsches Elektronen-Synchrotron (DESY), 22603 Hamburg, Germany, ^bCryogenic Ltd, London W3 7QE, UK,

^cDivision of Materials Sciences and Engineering (DMSE), Ames Laboratory, US DOE, Ames, IA 50010, USA,

^dHochfeld-Magnetlabor Dresden (HLD), Helmholtz-Zentrum Dresden-Rossendorf, D-01314 Dresden, Germany,

^eDepartment of Materials Science and Engineering, Iowa State University, Ames, IA 50011, USA, and

^fDepartment of Physics and Astronomy, Iowa State University, Ames, IA 50011, USA.

*Correspondence e-mail: sonia.francoual@desy.de

The resonant scattering and diffraction beamline P09 at PETRA III at DESY is equipped with a 14 T vertical field split-pair magnet. A helium-3 refrigerator is available that can be fitted inside the magnet's variable-temperature insert. Here the results of a series of experiments aimed at determining the beam conditions permitting operations with the He-3 insert are presented. By measuring the tetragonal-to-orthorhombic phase transition occurring at 2.1 K in the Jahn–Teller compound TmVO_4 , it is found that the photon flux at P09 must be attenuated down to 1.5×10^9 photons s^{-1} for the sample to remain at temperatures below 800 mK. Despite such a reduction of the incident flux and the subsequent use of a Cu(111) analyzer, the resonant X-ray magnetic scattering signal at the Tm L_{III} absorption edge associated with the spin-density wave in $\text{TmNi}_2\text{B}_2\text{C}$ below 1.5 K is intense enough to permit a complete study in magnetic field and at sub-Kelvin temperatures to be carried out.

1. Introduction

Single-crystal X-ray diffraction and resonant X-ray scattering are extremely valuable techniques for studying crystallographic phase transitions and other ordering phenomena such as orbital, multipolar or magnetic ordering as well as charge-density waves. These ordering phenomena usually show peculiar phase diagrams as a function of temperature, magnetic field or pressure and require that X-ray scattering experiments are made possible on samples subject to these external thermodynamic parameters. In the hard X-ray range, recent instrumental trends at third-generation synchrotron sources have been to push the feasibility of X-ray diffraction experiments in very high magnetic fields either using commercial superconducting (SC) magnets delivering permanent fields up to 17 T (Katsumata, 2005; Holmes *et al.*, 2012; Stempfer *et al.*, 2013) or developing pulsed field technology magnets producing peak fields of 30 T and beyond for a few milliseconds (Islam *et al.*, 2012; Duc *et al.*, 2014; Narumi *et al.*, 2012). For what concerns the establishment of extremely low temperatures, a wide variety of cryostats are nowadays commercially available that permit temperatures down to 4.2 K to be achieved during X-ray experiments. Temperatures down to 1.5 K can be reached using special cryostats (Brückel *et al.*, 1996) or SC magnets equipped with a ^4He variable-temperature insert (VTI). However, while the technology to achieve sub-Kelvin temperatures is well established at neutron



scattering facilities, *i.e.* the use of dilution refrigerators and ^3He cold fingers, X-ray studies combined with such sample environments are very seldom at synchrotron or laboratory X-ray sources (Nakajima *et al.*, 1995; Christiansen *et al.*, 1996; Katsumata, 2005). One of the reasons for this is the low penetration depth of X-rays which imposes windows to be installed made out of low-absorbing but unfriendly materials like beryllium. Another reason is that local heating of the sample already occurs at temperatures below 100 K due to the high heat load of synchrotron X-ray beams. This imposes the photon flux to be reduced by one or two orders of magnitude depending on the incoming X-ray flux and depending on whether exchange gas is present or not in order to remain at base temperature. In the sub-Kelvin range, higher attenuation factors are expected.

In this article we describe principles of operation of the ^3He insert at beamline P09 at the PETRA III storage ring and show that resonant X-ray magnetic scattering experiments are possible down to 360 mK in the hard X-ray range at a third-generation synchrotron source.

2. Helium-3 insert

Beamline P09 at the PETRA III storage ring is dedicated to resonant scattering and diffraction experiments in the hard X-ray range between 2.7 and 24 keV (Stempffer *et al.*, 2013). It is equipped with a 14 T vertical field split-pair magnet that can be mounted on the heavy-load non-magnetic Huber six-circle diffractometer present in the second experimental hutch. The magnet is equipped with a ^4He VTI operating at temperatures between 1.5 and 300 K and with successive beryllium and mylar windows allowing full optical access in the horizontal scattering plane. The closed-cycle ^3He fridge is a top-loading 2 m-long insert custom-designed by Cryogenic Ltd to fit inside the 2.5 cm-diameter bore of the VTI. The sample holder is attached at the bottom of the ^3He pot and cooled down by conduction. The sample holder and ^3He pot are enclosed in an inner vacuum chamber (IVC) while the mini and main sorption pumps lie in the main VTI space. The IVC is equipped with a 1 mm-thick beryllium window over 360° opening and 28 mm height which makes it possible to mount several samples at once on the same holder. The IVC is loaded with a few mbar of ^4He exchange gas at the start of operation which helps to cool the whole probe to base temperature using the cooling power of the VTI. Varying the temperature of the charcoal mini sorption pump (mini sorb) allows it to control the amount of ^4He exchange gas into the IVC: at base temperature the ^4He is completely removed so as to isolate thermally the ^3He pot from the IVC. The charcoal main sorption pump (main sorb) controls the absorption and desorption of ^3He gas from the main dump hence the amount of ^3He condensing into the ^3He pot. Varying the temperature of the main sorb allows it to vary the pumping pressure on the liquid ^3He and therefore also the temperature of the ^3He pot.

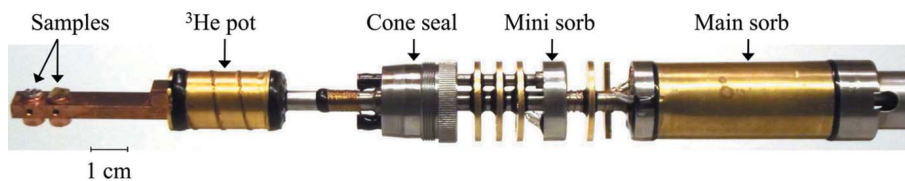


Figure 1 Bottom of the ^3He probe with the IVC removed where the samples, ^3He pot, main and mini sorption pumps can be seen.

The ^3He pot, main sorb and mini sorb are equipped with separate sensors and heaters. The ^3He pot temperature sensor is a CX1030 calibrated in magnetic field and temperature. Fig. 1 shows a photograph of the helium-3 probe with IVC removed, indicating the positions of the samples mounted on an oxygen-free Cu holder, the ^3He pot, the main and the mini sorb. The ^3He probe, VTI and magnet are controlled through a Labview program provided by Cryogenic Ltd. A dedicated Tango server establishes the communication between the PETRA III command line interface and this control software allowing for a complete remote control of all experimental variables.

For the present set of experiments, the VTI was maintained at a temperature of 1.9 K and the ^4He flow maintained at 12 mbar. About 10 mbar ^4He exchange gas was loaded into the IVC. Once the ^3He had condensed into the ^3He pot and the base temperature was achieved, the temperature was controlled by varying the temperature of the main sorb while keeping the mini sorb cold. Continuous operation for about 8–12 h was possible. Then, a recondensation was required taking about 40 min. The temperature of the sample was monitored first by a commercial Cernox thermometer CX1030 from Lakeshore positioned close to the sample, and then by a CX1050SD sensor calibrated in a Quantum Design PPMS equipped with a ^3He low-temperature stage at the HLD. The two CX1030 sensors (sample and ^3He pot) systematically returned the same temperature pointing to the absence of any thermal gradient over the sample holder. However, only the CX1050SD thermometer returned the transition temperatures reported for the samples in the literature. After calibrating the CX1030 sensors *versus* the CX1050 sensor, the following correction, $T = 0.06999 + 0.89643T_{\text{CX1030}}$, was systematically applied to the temperature returned by the CX1030 sensors in zero field. In Fig. 2 we show a typical dependence of the temperature of the ^3He pot *versus* the temperature of the main sorb during operation. The base temperature is 360 mK and the maximum temperature achieved here is 3 K. The temperature follows a sigmoidal trend in between these two extrema. The temperature dependence shown on Fig. 2 was found very reproducible for subsequent beam times. For measurements in the presence of a magnetic field, the magnetoresistance of the CX1030 thermometers has been fully characterized by Cryogenic Ltd. Henceforth, the zero field temperature can be retrieved. Since magnetic fields of 14 T induce temperature errors $\Delta T/T$ of the Cernox sensors of less than 1% at temperatures between 4 K and 20 K, the temperature of the main sorb does not need to be corrected

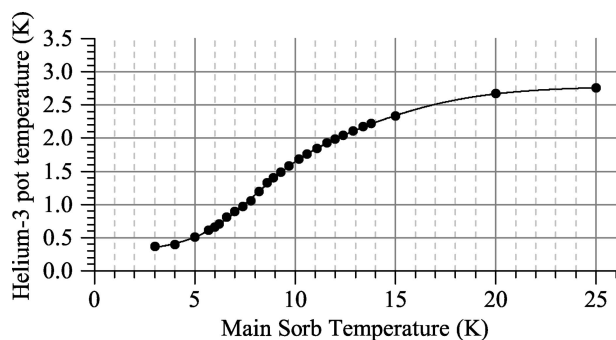


Figure 2
Temperature of the helium-3 pot as a function of the main sorb temperature.

for magnetic fields in this temperature range. On the other hand, since $\Delta T/T$ at 14 T is higher than 10% at temperatures below 1.4 K, the sample temperature must be corrected. This is done automatically within the temperature control software.

3. Validating measurements

3.1. Jahn–Teller effect in TmVO_4

The rare-earth vanadate TmVO_4 undergoes a cooperative Jahn–Teller distortion at temperatures below $T_c = 2.1$ K, where the degeneracy of the electronic ground state of the Tm^{3+} ion is lifted by a crystallographic distortion (Cooke *et al.*, 1970; Becker *et al.*, 1972). Details of the tetragonal-to-orthorhombic second-order phase transition have been studied by X-ray diffraction on a single-crystal down to 1.7 K by Segmüller *et al.* (1974) at a laboratory X-ray source immersing the sample in a ^4He bath and more recently by Suzuki *et al.* (2002) on a powder sample down to 250 mK at a laboratory X-ray source using a ^3He – ^4He dilution refrigerator. The principal axes of distortion are $[110]$ and $[1, -1, 0]$. The $(h, h, 0)$ diffraction lines in the high-temperature state split into two lines $(2h, 0, 0)$ and $(0, 2h, 0)$ below T_c . The splitting varies continuously between 0.80 K and 2.15 K, making TmVO_4 an appropriate reference compound to investigate beam heating effects at those low temperatures.

The TmVO_4 single-crystal used in the present experiment was grown to a length of 12 cm and diameter of 8 mm by the optical floating zone technique at the DSME at Ames Laboratory. It was subsequently cut at DESY so as to obtain two parallel flat faces normal to the $(1, 1, 0)$ direction. The sample surface was then highly polished in order to remove any surface damage. The sample, 1.5 mm thick and with $3.2 \text{ mm} \times 2.5 \text{ mm}$ cross section, was glued with GE-varnish and mounted so that the $(1, 1, 0)$ and $(1, -1, 0)$ reciprocal lattice directions were aligned in the horizontal scattering plane. The X-ray diffraction measurements were carried out at an incident energy of 8.664 keV and with a beam size of $200 \mu\text{m} \times 70 \mu\text{m}$ ($H \times V$) at the sample position. Higher harmonics were suppressed by mirrors and additional detuning of the monochromator. The detector horizontal slits were closed down so as to resolve the peak splitting. With an

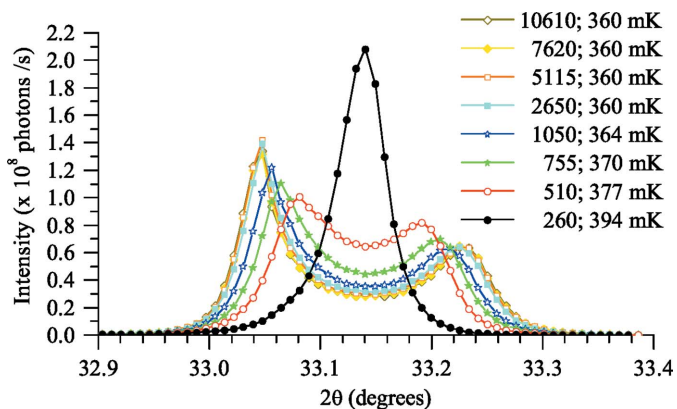


Figure 3
 θ – 2θ scans about the (220) Bragg reflection of the TmVO_4 tetragonal phase for decreasing attenuation factor of the incident beam between 10^6 and 10^2 and the helium-3 pot maintained at a base temperature of 360 mK. Intensities are corrected by the monitor and the attenuation factor. The attenuation factor at which the scans were recorded and the temperature returned by the thermometer are indicated in the legend.

incident X-ray photon flux at P09 of about 1.5×10^{13} photons s^{-1} at this energy (Stremper *et al.*, 2013) and considering the intensity reduction by the detuning and the attenuation of the incident beam by the magnet and IVC Be windows, the heat load on the sample is 13.1 mW. Calibrated attenuator foils upstream of the magnet were used to decrease the photon flux and the heat load on the sample. Independently of how much flux impinges on the sample, 99.99% (99%) of it is absorbed within a $67 \mu\text{m}$ ($34 \mu\text{m}$) depth due to the high absorption coefficient of the sample at this photon energy.

In Fig. 3 we show θ – 2θ scans through the (220) Bragg reflection of the TmVO_4 tetragonal phase for decreasing incident beam attenuation factor of the incident beam between 10^6 and 10^2 . The ^3He pot, main sorb and mini sorb were maintained at the base temperatures of 360 mK, 4 K and 3 K, respectively. The intensities are corrected by the monitor and attenuation factor values. The increasing local heating of the sample causes the $(4, 0, 0)$ and $(0, 4, 0)$ reflections of the orthorhombic phase to merge into the single $(2, 2, 0)$ reflection of the tetragonal phase at attenuation factors lower than 300, indicating that the sample temperature exceeds T_c at these photon fluxes. For attenuation factors larger than 5000, there is no noticeable change in the peak positions, indicating that the sample temperature is lower than 0.8 K. Note that the temperature of the sensor shows only a small deviation of a few tens of mK from a base temperature of 360 mK over the whole attenuation range. The peak splitting between the $(4, 0, 0)$ and $(0, 4, 0)$ reflections was investigated as a function of temperature with an attenuation factor of 10^5 (equivalent heat load of $0.12 \mu\text{W}$) in order to rule out any beam heating effects. In Fig. 4 we show the associated static strain $e_2/2 = (a - b)/a_0$ as a function of temperature together with the results reported by other groups (Segmüller *et al.*, 1974; Suzuki *et al.*, 2002). As can be seen, all X-ray data compare well. Fig. 4 can be used to estimate the temperature of the sample in Fig. 3. In Fig. 5 we plot the static strain of the sample as a function of the logarithm of the attenuation factor and the associated true

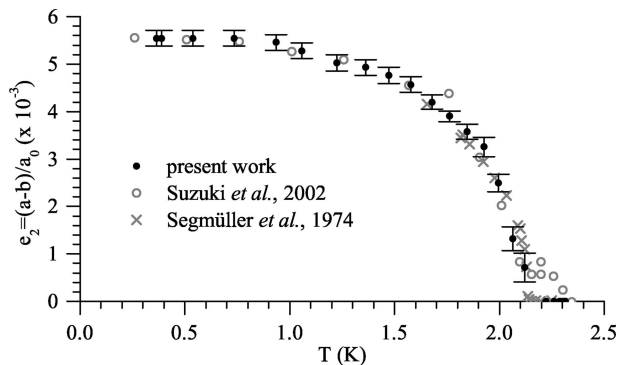


Figure 4
Static strain $(a - b)/a_0$ as a function of temperature obtained in the present work compared with that reported by Segmüller *et al.* (1974) and Suzuki *et al.* (2002).

temperature. From a power fit through the data points, we find that an attenuation factor of the incident beam of 3500 is required to maintain the sample at temperatures below 1 K which corresponds to a beam heat load of 3.7 μ W. A power-law extrapolation to lower temperatures suggests that an attenuation factor of 10^4 (3×10^4) is required to maintain the sample at temperatures below 700 mK (500 mK).

3.2. Spin-density wave in $\text{TmNi}_2\text{B}_2\text{C}$

The rare-earth nickel borocarbides $\text{RENi}_2\text{B}_2\text{C}$ (RE = Tm, Ho, Er, Dy) with body-centered tetragonal $I4/mmm$ crystal structure (Lynn *et al.*, 1997) have attracted much attention since their discovery in 1994 (Gupta *et al.*, 1994; Canfield *et al.*, 1998) because of the coexistence of superconductivity and antiferromagnetism at low temperatures. In $\text{TmNi}_2\text{B}_2\text{C}$, superconductivity sets in at 11 K and coexists with an antiferromagnetic order below $T_N = 1.5$ K (Movshovich *et al.*, 1994). The magnetic structure has been investigated in detail by neutron diffraction down to 0.1 K in magnetic fields up to 6 T (Nørgaard Toft *et al.*, 2004) and by resonant X-ray magnetic scattering (RXMS) down to 0.9 K (Mannix *et al.*, 2004) at the XMaS UK CRG bending-magnet beamline at ESRF using a Displex cryostat equipped with a Joule Thompson (JT) stage flowing ^3He through the JT stage. The

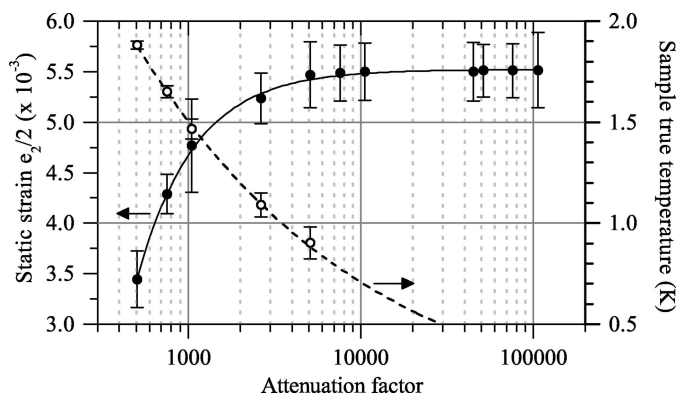


Figure 5
Static strain (left axis) and temperature of the sample (right axis) as a function of the logarithm of the attenuation factor.

Tm moments are aligned along the tetragonal c -axis forming an incommensurate spin-density wave (SDW) with ordering wavevector $(0.094, 0.094, 0)$ and with an ordered magnetic moment on the Tm site of 3.78 μB at 360 mK (Lynn *et al.*, 1997). For a magnetic field applied along the tetragonal a -axis, the ordering wavevector changes to $(0.483, 0, 0)$ at 1 T and to $(0.496, 0, 0)$ at 4 T.

Measurements at P09 were carried out using the same experimental set-up as described for TmVO_4 in the previous section. The $\text{TmNi}_2\text{B}_2\text{C}$ sample is one previously used in a high-energy X-ray diffraction study at beamline BW5 at the DORIS storage ring at DESY (Andersen *et al.*, 2006). The single-crystals are grown out of excess Ni_2B solution in a novel two-step process (Canfield & Fisher, 2001). The single-crystals grow as plates with the c -axis being perpendicular to the surface. The sample was oriented with the $(1, 1, 0)$ and the $(0, 0, 1)$ crystallographic axes in the horizontal scattering plane. This allows probing of the first-order magnetic satellites along the $(1 + \tau, 1 + \tau, 10)$ reciprocal lattice direction and investigation of the magnetic field effects for the field applied along the $(1, -1, 0)$ crystallographic axis. In this geometry the incident X-rays are π polarized, *i.e.* the polarization vector lies in the scattering plane. The polarization of the scattered signal was analyzed using a $\text{Cu}(1, 1, 1)$ crystal with 10% reflectivity. Linear polarization scans (Scagnoli *et al.*, 2009) were carried out using two 400 μm diamond quarter-wave plates in series in 90° geometry (Stempffer *et al.*, 2013; Francoual *et al.*, 2013). All measurements were carried out with an equivalent attenuation factor of 10^4 .

In Fig. 6 we show a reciprocal-space scan along the $(1 + \tau, 1 + \tau, 10)$ direction at 360 mK in the $\pi\sigma'$ channel at the resonant energy of 8.654 keV close to the Tm L_{III} edge. A non-zero signal is fully resolved peaking at $\tau = 0.0956$ r.l.u. with an intensity at maximum of 25 counts counting 10 s per point. In Figs. 7(a) and Fig. 7(b) we show the results of a full polarization analysis of the magnetic superlattice peak and of the neighboring $(1, 1, 10)$ charge Bragg reflection carried out at base temperature. The Stokes parameters of the scattered beam, P'_1 and P'_2 , are plotted as a function of the angle of linear polarization of the incident beam η . The Stokes parameters for the Bragg peak are fitted considering the expressions given for P'_1 and P'_2 in the case of Thomson charge

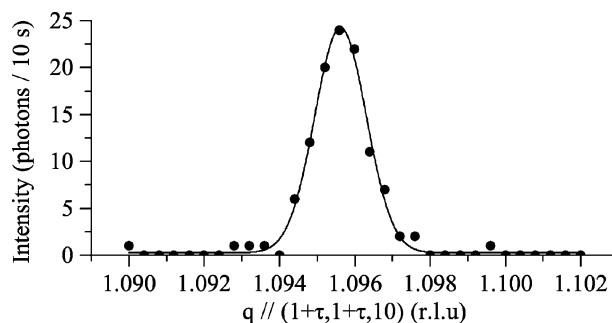
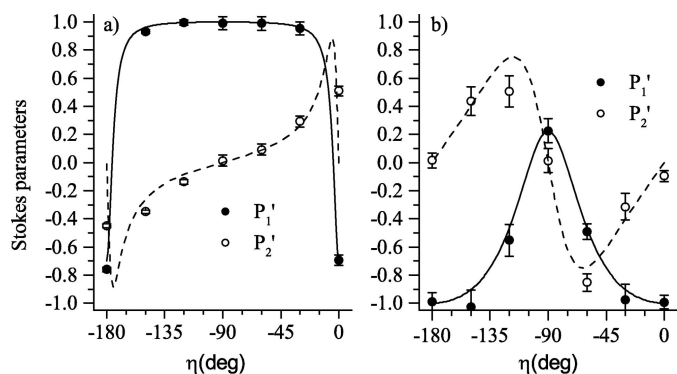


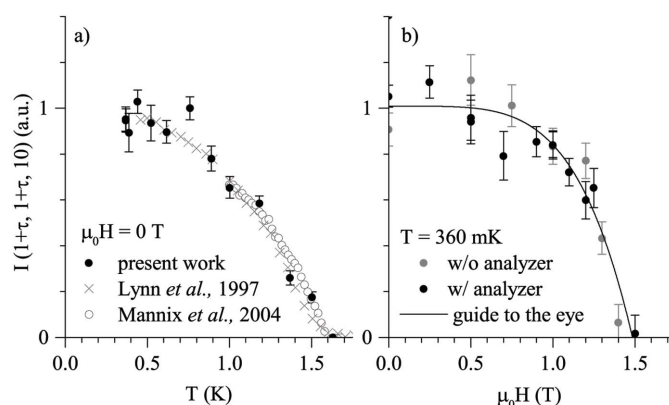
Figure 6
 q -scan along the $(1 + \tau, 1 + \tau, 10)$ reciprocal lattice direction at base temperature in $\text{TmNi}_2\text{B}_2\text{C}$ measured in the $\pi\sigma'$ channel with an attenuation factor of 10^4 at the resonant energy of 8.654 keV.


Figure 7

Stokes parameters P_1' and P_2' as a function of the angle of incident linear polarization η at base temperature (a) for the (1,1,10) Bragg peak and (b) for the $(1+\tau, 1+\tau, 10)$ magnetic peak. The solid and dashed lines are the computed values for P_1' and P_2' , respectively, considering a charge scattering process at the charge Bragg peak and a resonant scattering dipole process at the magnetic Bragg peak assuming that the magnetic moment is aligned along c . The only fitting parameter is the degree of incident polarization, which is set to vary as a sine wave as a function of η (see text).

scattering by Detlefs *et al.* (2012). In the horizontal scattering geometry, the Stokes parameters of the incident beam write as $P_1 = -P_{\text{LIN}} \cos(2\eta)$ and $P_2 = -P_{\text{LIN}} \sin(2\eta)$, with $P_{\text{LIN}} = (P_1^2 + P_2^2)^{1/2}$. The Stokes parameters for the magnetic peak are computed considering the Jones matrix for resonant electric dipole exchange scattering given by Hill & McMorro (1996). In the $(\mathbf{u}_1, \mathbf{u}_2, \mathbf{u}_3)$ coordinates system used in X-ray magnetic scattering experiments (Blume & Gibbs, 1988; Hill & McMorro, 1996; Detlefs *et al.*, 2012), the components of the magnetic moment can be written as $S_1 = S \sin(\alpha) \cos(\psi)$, $S_2 = S \sin(\alpha) \sin(\psi)$ and $S_3 = S \cos(\alpha)$. For a magnetic moment aligned along the c tetragonal axis and for a scattering vector of (1.0956, 1.0956, 10), the polar angle α is $180 + 25.20^\circ$ and the azimuthal angle ψ is 0° . The degree of incident linear polarization, P_{LIN} , is made to vary with η as a sine wave with 90° periodicity and 45° phase in accordance with known characteristics for the double phase-retarder set-up at P09 (Francoual *et al.*, 2013). In Figs. 7(a) and Fig. 7(b) we plot with solid lines the computed values for P_1' and P_2' for the two different scattering processes for $P_{\text{LIN}} = 0.91525 + 0.08225 \sin(2\eta + \pi/2)$. As can be seen, an excellent fit of the data is obtained which allows it to confirm the magnetic structure previously reported for $\text{TmNi}_2\text{B}_2\text{C}$ (Nørgaard Toft *et al.*, 2004).

The $(1+\tau, 1+\tau, 10)$ peak (Fig. 6) was investigated as a function of temperature at several different magnetic fields and as a function of magnetic field at several different temperatures by performing systematic q -scans along the scattering vector. The resulting integrated intensity $I(1+\tau, 1+\tau, 10)$ is shown as a function of temperature for $\mu_0 H = 0$ T in Fig. 8(a) and as a function of magnetic field for $T = 360$ mK in Fig. 8(b). The reconstructed $(\mu_0 H, T)$ phase diagram is shown Fig. 9. The temperature dependence of the integrated intensity is in good agreement with previous reports (Lynn *et al.*, 1997; Mannix *et al.*, 2004) in the full temperature range as shown in Fig. 8(a). The spin-density wave is suppressed at 1.6 K at zero field and at 1.4 T at zero


Figure 8

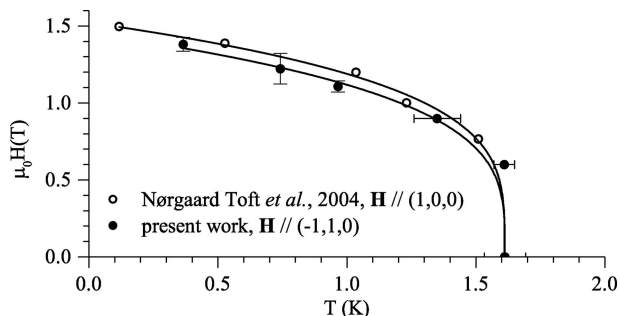
(a) Integrated intensity $I(1+\tau, 1+\tau, 10)$ as a function of temperature in zero field compared with the neutron results from Lynn *et al.* (1997) and the RXMS results from Mannix *et al.* (2004). (b) Integrated intensity $I(1+\tau, 1+\tau, 10)$ as a function of magnetic field at 360 mK.

temperature as extrapolated from Fig. 9. Here, the critical field for the field along $(1, -1, 0)$ is slightly lower than the one reported for the field applied along the $(1, 0, 0)$ direction (Nørgaard Toft *et al.*, 2004) which suggests a basal plane anisotropy. The error bars in Figs. 8(a) and 8(b) amount to 7% and 9% counting 20 s and 10 s per point, respectively. A 3% standard deviation would require counting 150 s per point for this sample and particular magnetic peak.

The reasonable signal-to-noise ratio obtained for the RXMS intensity in Fig. 6 together with the good quality of the data and the fits in Fig. 7(b) show that the helium-3 fridge described in §2 can be used to carry out RXMS studies in the sub-Kelvin temperature range despite the necessary reduction of the incident X-ray flux. Furthermore, the results shown in Figs. 8(b) and Fig. 9 demonstrate its usability in high magnetic fields.

4. Discussion

Heating by the synchrotron X-ray beam has been the object of detailed calculations and detailed experimental determinations mostly for biological samples immersed in a cooling gas stream (Mhaisekar *et al.*, 2005; Snell *et al.*, 2007, and references


Figure 9

$(\mu_0 H, T)$ phase diagram of the spin-density wave in $\text{TmNi}_2\text{B}_2\text{C}$ for the magnetic field applied along $(-1, 1, 0)$ (filled circles) as determined in the present work and for the magnetic field applied along $(1, 0, 0)$ (empty circles) as reported by Nørgaard Toft *et al.* (2004). The solid lines are guides to the eye.

therein). In these models, the sample is cooled down by convection and its size is usually small compared with the X-ray attenuation length so that not all of the beam power is absorbed into the sample. Two temperatures are computed: the temperature of the outside surface of the crystal and the temperature inside. While the external temperature is altered by parameters such as the crystal size and the gas velocity, the internal temperature is influenced by the sample thermal conductivity and the beam size. Both temperatures are shown to depend linearly on the incident flux (Mhaisekar *et al.*, 2005). For samples absorbing the full beam, more heat is generated internally and the temperature profile across the sample is less uniform (Kuzay *et al.*, 2001). The temperature rise ΔT on a 1 mm glass bead with $0.97 \text{ W m}^{-1} \text{ K}^{-1}$ thermal conductivity in a 290 K N_2 gas stream absorbing 3.37 mW beam power is 20 K (Snell *et al.*, 2007). ΔT increases to 80 K when the beam heat load is increased to 13.1 mW. In the set-up presented here, the heat balance problematic is different because the sample sits in a vacuum, it is cooled by conduction and only one of its sides is in contact with the cold surface. The outer surfaces lose energy by radiative transfer mechanisms, convection being absent due to the absence of exchange gas. Nevertheless, temperature increases in the same order of magnitude are expected from previous experiments using Displex closed-cycle cryostats. In the filled skutterudite $\text{PrRu}_4\text{P}_{12}$, the superlattice peaks associated with the transition at 60 K are invisible at a 5.5 K nominal temperature of the cryostat unless attenuating the incident beam by at least a factor of 20 at beamline P09 at 5962 eV (unpublished results). With the helium-3 fridge, we find a TmVO_4 sample temperature of 1.9 K and 1.1 K for an incident beam of $26 \mu\text{W}$ (attenuation factor 500) and $5 \mu\text{W}$ (attenuation factor 2650), respectively (Fig. 5). The dependence of the temperature rise on the incident flux is smaller than linear, which might be due to the combined effect of an increased sample thermal conductivity with decreased temperature and an increased cooling power at beam heat loads coming close to $25 \mu\text{W}$. All thermometers show very little variation in their read-outs from the base temperature of 360 mK for beam heat loads up to $5 \mu\text{W}$ demonstrating that the beam heating is localized in that very narrow region around where the beam hits the sample. The temperature difference ΔT of 0.74 K between the sample temperature and the ^3He pot temperature for $5 \mu\text{W}$ deposited energy is important, suggesting that the heat transfer is not very effective. The rate of heat transfer to the cold finger depends on the thermal conductivity κ of the sample, its absorption properties, its thickness and the quality of the thermal contact between the sample and the sample holder. TmVO_4 is a poor thermal conductor with $\kappa = 0.1 \text{ W m}^{-1} \text{ K}^{-1}$ at 1 K and $0.02 \text{ W m}^{-1} \text{ K}^{-1}$ at 360 mK (Daudin *et al.*, 1980). Furthermore, the sample used in our study is quite thick ($\sim 1.5 \text{ mm}$). We expect a lower ΔT for thinner samples, for samples with higher thermal conductivity and for less absorbing materials. For instance, $\text{TmNi}_2\text{B}_2\text{C}$ has $0.35 \text{ W m}^{-1} \text{ K}^{-1}$ thermal conductivity at 1 K (Hennings *et al.*, 2002). Its attenuation length, μ_{att} , is 1.64 times shorter than that of TmVO_4 at the Tm L_{III} absorption edge. According to

Fourier's law of heat conduction, the dependence of ΔT on κ is linear. Assuming the dependence of ΔT on μ_{att} to be linear (Mhaisekar *et al.*, 2005), the temperature of a $\text{TmNi}_2\text{B}_2\text{C}$ sample of a similar shape as the TmVO_4 sample used hereby would be 0.7 K rather than 1.1 K for a $5 \mu\text{W}$ beam heat load. The precise dependence of ΔT on ξ , μ_{att} and on the conduction shape factor are to be determined either numerically or empirically.

The nominal cooling power of the helium-3 refrigerator is $25 \mu\text{W}$ at 360 mK, $50 \mu\text{W}$ at 400 mK and $125 \mu\text{W}$ at 500 mK. The probe and sample thermometers behave in line with this, as shown in Fig. 3, *i.e.* they show a temperature of 400 mK for $50 \mu\text{W}$ incoming heat load. This means that the beam heat load needs to be attenuated at least down to $25 \mu\text{W}$ in order to avoid any rapid warm-up of the probe and ensure a long enough time window between two successive condensation cycles. We find that a beam heat load of $1.3 \mu\text{W}$ (attenuation factor 10^4) guarantees continuous operation between 8 and 12 h, whereas at attenuation factors of the order of 10^3 this time window is reduced to about 3 h. Therefore, independently of which sample is mounted onto the probe, an attenuation of the beam of four orders of magnitude is also required at P09 to ensure long operation of the helium-3 refrigerator.

Our study raises the long-standing issue about how to determine the true temperature of a sample in a low-temperature X-ray experiment when the sample is enclosed in a cryostat. As we have shown, thermometers are ineffective at measuring the temperature rise in that narrow region where the beam hits the sample. The best method is to use the X-ray probe to measure a quantity that has a known relationship to the temperature. For instance, Christiansen *et al.* (1996) have been able to return the true temperature of the sample by fitting the temperature dependence of the X-ray magnetic circular dichroism signal in plastocyanin as a function of magnetic field to the one expected for an isotropic $S = 1/2$ spin system. Wang *et al.* (2012) have used instead the imbalance between Stokes and anti-Stokes intensities in nuclear resonant vibrational X-ray spectroscopy. In this work, we have measured the peak splitting coming along with a crystallographic distortion to determine the true sample temperature in TmVO_4 . During X-ray diffraction experiments, the real temperature experienced by the sample is usually checked by measuring the temperature dependence of a characteristic peak that appears below a known critical temperature T_c and comparing the temperature returned by the thermometer for that transition temperature with T_c . Unless the temperature rise ΔT is temperature independent as shown by Snell *et al.* (2007) for a glass bead between 220 and 290 K, this method allows it to determine ΔT and which attenuation factor of the incident beam to use only at T_c . Henceforth, it might be good practice to carry out a series of measurements attenuating by one more order of magnitude than has been determined experimentally and check for discrepancies.

A previous experimental study combining a synchrotron X-ray beam and a dilution refrigerator has concluded that ultralow-temperature experiments are better combined with a

laboratory X-ray source (Suzuki *et al.*, 2002). This is overlooking all the advantages of using a synchrotron X-ray beam, for instance the energy tunability and the polarization control of the X-ray beam, which permit investigation of the magnetic properties of materials (Lovesey & Collins, 1996). Furthermore, the higher flux at synchrotron sources enables insertion of additional optical devices into the X-ray beam before the sample such as a double-phase retarder for full polarization control of the incident X-ray beam, an X-ray beam diagnostic unit for polarization monitoring or compound refractive lenses for the purpose of focusing, as is done at beamline P09. We have proven hereby that a complete resonant X-ray magnetic X-ray scattering study is possible at sub-Kelvin temperatures at beamline P09. Both the resonant and non-resonant magnetic scattering intensities at first-harmonic satellites depend quadratically on the magnetic moment (Hill & McMorro, 1996; Blume & Gibbs, 1988) and on the number of magnetic atoms in the unit cell. In $\text{TmNi}_2\text{B}_2\text{C}$, the ordered magnetic moment on the Tm site is $3.78 \mu\text{B}$ at 360 mK (Lynn *et al.*, 1997) and there are two magnetic atoms per unit cell. The resonant enhancement of the magnetic scattering intensities at the L_{II} and L_{III} edges of the $4f$ lanthanide elements varies between 1 and 2500 for electric dipole $E1$ transitions and is the strongest for gadolinium and holmium (Hamrick, 1990). For thulium, the resonant enhancement is modest, of the order of 50 (Bohr *et al.*, 1990). Even stronger resonant enhancements of the order of 3000 are expected for $E1$ transitions at the L_{II} and L_{III} edges of the $5d$ transition elements, at X-ray energies between 9.2 and 14.2 keV, as is exemplified in K_2ReCl_6 (McMorro *et al.*, 2003). At the M_{IV} and M_{V} edges of the $5f$ actinide elements, at X-ray energies between 3.3 and 3.9 keV, enhancements of the order of 10^8 are even achieved (Hamrick, 1990). In $\text{TmNi}_2\text{B}_2\text{C}$, the count rate is $2.5 \text{ counts s}^{-1}$ at 8.654 keV at 360 mK using a Cu(111) analyzer with 10% efficiency and an attenuation factor of 10^4 . At a lower energy, the output count rate may be significantly altered due to absorption by the magnet and IVC windows. 3.7 times less intensity is transmitted at 5.5 keV than at the Tm L_{III} edge and 1000 times less at 3.5 keV. Also, though the beam power decreases ($\propto \lambda_X^{-1}$), the photoelectric absorption increases slightly faster ($\propto Z^n \lambda_X^3$, $n \in [3, 4]$), bringing larger attenuation lengths, and the incident flux might further need to be reduced by a factor of ten in some extreme cases depending on the material. Yet these numbers are not prohibitive in light of the aforementioned resonant enhancements. Henceforth, $\text{TmNi}_2\text{B}_2\text{C}$ is not a unique scientific case for which resonant X-ray magnetic scattering at helium-3 temperatures might be carried out successfully.

5. Conclusions

Beamline P09 at PETRA III at DESY is equipped with a helium-3 fridge that can be inserted into the variable-temperature insert of the 14 T magnet for the purpose of single-crystal X-ray diffraction and resonant X-ray magnetic scattering experiments. The helium-3 fridge insert has been commissioned and is now fully operational, permitting user-

friendly experiments at temperatures between 0.4 K and 3 K in magnetic fields up to 14 T in a wide range of scattering angles. Beam heating effects have been fully characterized: an attenuation factor of the incident beam of 10^4 is needed to ensure that the sample is at temperatures below 800 mK and that the helium-3 fridge remains cold for more than 10 h.

Acknowledgements

The research presented here was carried out at the light source PETRA III at DESY, a member of the Helmholtz Association (HGF). The authors would like to thank R. Döring, M. Spiwek and D. Reuther for technical and engineering support. The single crystals of TmVO_4 and $\text{TmNi}_2\text{B}_2\text{C}$ were grown at Ames Laboratory. The work was supported by the US Department of Energy, Office of Basic Energy Sciences, Materials Science and Engineering Division. Ames Laboratory is operated for the US Department of Energy by Iowa State University under Contract No. DE-AC02-07CH11358.

References

- Andersen, N. H., Jensen, J., Jensen, T. B. S., Zimmermann, M. v., Pinholt, R., Abrahamsen, A. B., Toft, K. N., Hedegård, P. & Canfield, P. C. (2006). *Phys. Rev. B*, **73**, 020504.
- Becker, P. J., Tyte, R. N. & Leask, M. J. M. (1972). *J. Appl. Cryst.* **5**, 2027–2036.
- Blume, M. & Gibbs, D. (1988). *Phys. Rev. B*, **37**, 1779–1789.
- Bohr, J., Gibbs, D. & Huang, K. (1990). *Phys. Rev. B*, **42**, 4322–4328.
- Brückel, T., Nowak, R., Köhler, T., Brüggemann, U., Maul, U., Pfützenreuter, E., Rilling, V. & Prandl, W. (1996). *J. Appl. Cryst.* **29**, 686–691.
- Canfield, P. C. & Fisher, I. R. (2001). *J. Cryst. Growth*, **225**, 155–161.
- Canfield, P. C., Gammel, P. L. & Bishop, D. J. (1998). *Phys. Today*, **51**, 40–46.
- Christiansen, J., Peng, G., Young, A. T., LaCroix, L. B., Solomon, E. I. & Cramer, S. P. (1996). *Inorg. Chim. Acta*, **243**, 229–232.
- Cooke, A. H., Ellis, C. J., Gehring, K. A., Leask, M. J. M., Martin, D. M., Wanklyn, B. M., Wells, M. R. & White, R. L. (1970). *Solid State Commun.* **8**, 689–692.
- Daudin, B., de Goër, A. M. & Smith, S. H. (1980). *Phonon Scattering in Condensed Matter*, edited by Humphrey J. Maris, pp. 93–96. New York: Plenum Press.
- Detlefs, C., Sanchez del Rio, M. & Mazzoli, C. (2012). *Eur. Phys. J. Spec. Top.* **208**, 359–371.
- Duc, F., Fabrèges, X., Roth, T., Detlefs, C., Frings, P., Nardone, M., Billette, J., Lesourd, M., Zhang, L., Zitouni, A., Delescluse, P., Béard, J., Nicolin, J. & Rikken, G. L. (2014). *Rev. Sci. Instrum.* **85**, 053905.
- Francoual, S., Stempffer, J., Reuther, D., Shukla, D. & Skaugen, A. (2013). *J. Phys. Conf. Ser.* **425**, 132010.
- Gupta, L. C., Nagarajan, R., Godart, C., Dhar, S. K., Mazumdar, C., Hossain, Z., Levy-Clement, C., Padalia, B. d. & Vijayaraghavan, R. (1994). *Physica C*, **235–240**, 150–153.
- Hamrick, M. D. (1990). Thesis, Rice University, USA.
- Hennings, B. D., Naugle, D. G. & Canfield, P. C. (2002). *Phys. Rev. B*, **66**, 214512.
- Hill, J. P. & McMorro, D. F. (1996). *Acta Cryst.* **A52**, 236–244.
- Holmes, A. T., Walsh, G. R., Blackburn, E., Forgan, E. M. & Savey-Bennett, M. (2012). *Rev. Sci. Instrum.* **83**, 023904.
- Islam, Z., Capatina, D., Ruff, J. P. C., Das, R. K., Trakhtenberg, E., Nojiri, H., Narumi, Y., Welp, U. & Canfield, P. C. (2012). *Rev. Sci. Instrum.* **83**, 035101.
- Katsumata, K. (2005). *Phys. Scr.* **71**, CC7–CC13.

- Kuzay, T. M., Kazmierczak, M. & Hsieh, B. J. (2001). *Acta Cryst.* **D57**, 69–81.
- Lovesey, S. W. & Collins, S. P. (1996). *X-ray Scattering and Absorption by Magnetic Materials*, *Oxford Series on Synchrotron Radiation*. Oxford: Clarendon Press.
- Lynn, J. W., Skanthakumar, S., Huang, Q., Sinha, S. K., Hossain, Z., Gupta, L. C., Nagarajan, R. & Godart, C. (1997). *Phys. Rev. B*, **55**, 6584–6598.
- McMorrow, D. F., Nagler, S. E., McEwen, K. A. & Brown, S. D. (2003). *J. Phys. Condens. Matter*, **15**, L59–L66.
- Mannix, D., Thompson, P., Brown, S., Bouchenoire, L. & Canfield, P. C. (2004). *Physica B*, **353**, 121–126.
- Mhaisekar, A., Kazmierczak, M. J. & Banerjee, R. (2005). *J. Synchrotron Rad.* **12**, 318–328.
- Movshovich, R., Hundley, M. F., Thompson, J. D., Canfield, P. C., Cho, B. K. & Chubukov, A. V. (1994). *Physica C*, **227**, 381–386.
- Nakajima, T., Ohta, J., Yonenaga, I., Koizumi, H., Iwasa, I., Suzuki, H., Suzuki, T. & Suzuki, H. (1995). *J. Appl. Cryst.* **28**, 375–384.
- Narumi, Y., Nakamura, T., Kinoshita, T., Matsuda, Y. H. & Nojiri, H. (2012). *Synchrotron Radiat. News*, **25**, 12.
- Nørgaard Toft, K., Abrahamsen, A. B., Eskildsen, M. R., Lefmann, K., Andersen, N. H., Vorderwisch, P., Smeibidl, P., Meissner, M. & Canfield, P. C. (2004). *Phys. Rev. B*, **69**, 214507.
- Scagnoli, V., Mazzoli, C., Detlefs, C., Bernard, P., Fondacaro, A., Paolasini, L., Fabrizi, F. & de Bergevin, F. (2009). *J. Synchrotron Rad.* **16**, 778–787.
- Segmüller, A., Melcher, R. L. & Kinder, H. (1974). *Solid State Commun.* **15**, 101–104.
- Snell, E. H., Bellamy, H. D., Rosenbaum, G. & van der Woerd, M. J. (2007). *J. Synchrotron Rad.* **14**, 109–115.
- Strempler, J., Francoual, S., Reuther, D., Shukla, D. K., Skaugen, A., Schulte-Schrepping, H., Kracht, T. & Franz, H. (2013). *J. Synchrotron Rad.* **20**, 541–549.
- Suzuki, H., Naher, S., Shimoguchi, T., Mizuno, M., Ryu, A. & Fujishita, H. (2002). *J. Low Temp. Phys.* **128**, 1–7.
- Wang, H., Yoda, Y., Kamali, S., Zhou, Z.-H. & Cramer, S. P. (2012). *J. Synchrotron Rad.* **19**, 257–263.